Understanding Shape and Residual Stress Dynamics in Rod-Like Plant Organs

Amir Porat[a,b,c,†]

[a]Sainsbury Laboratory, University of Cambridge, Bateman Street, Cambridge CB2 1LR, UK
[b]Department of Condensed Matter, School of Physics and Astronomy, Tel Aviv University, Tel Aviv 69978, Israel
[c]The Center for Physics and Chemistry of Living Systems, Tel-Aviv University, Tel Aviv 6997801, Israel
[†]amir.porat@slcu.cam.ac.uk

Residual stresses are common in rod-like plant organs such as roots and shoots. Such stresses can emerge from structural incompatibilities, which arise from the juxtaposition of layers of tissue with different intrinsic lengths. Although growth of individual plant cells is driven by mechanical stresses, the impact and role of tissue-scale internal residual stresses on shape dynamics at the organ scale remain poorly understood. Here, we introduce a novel theoretical framework in which the organ, described as a set of connected, concentric morphoelastic cylindrical shells representing distinct tissues, grows axially in response to its local elastic strain. This approach allows to formulate analytical expressions relating tissue-level differences in elasticity and intrinsic growth to macroscopic characteristics such as organ axial growth rates, bending motions, and residual stress profiles. To demonstrate the framework, we analyze a minimal two-layer model representing the epidermis and inner tissues, and use it to explore the "epidermal growth control" hypothesis, which posits that the epidermis regulates expansion by mechanically limiting inner tissue elongation. Our analysis also reveals a form of mechanical memory and accounts for observed phenomena such as autotropism.

Introduction

Slender, rod-like multicellular organs, such as roots and shoots, are ubiquitous in plants. Despite the crucial role of residual stresses in plant development (1–6), their influence on macroscopic growth-driven movements in roots and shoots remains inadequately understood. Several mechanisms can lead to axial residual stresses in plants (1). In addition to internal hydrostatic turgor pressure, which keeps cell walls taut (3, 7), residual stresses can emerge from structural incompatibilities. These arise when tissues with different intrinsic lengths exert forces on each other, due to either incompatible intrinsic growth rates (8), or tissue shrinkage as seen in plant tendrils and reaction wood (9–11) (see Fig. 1A). Recent mathematical models describe the morphogenesis of these organs using morphoelastic rods, focusing on their centerline - a one dimensional space-curve that spans their longest dimension, congruent to the axial growth direction (8, 12–14). Though these macroscopic models are successful in describing various movements, they often ignore elastic deformations (14–18), neglect feedback from mechanical deformations on growth (19–21), or average elastic fields over cross sections of the rod (12). Here, we examine how axial residual stress patterns within rod-like plant organs may emerge and influence macroscopic growth-driven movements. We describe the organ as a bundle of morphoelastic, concentric cylindrical shells (Fig. 1A,C), motivated by the internal architecture of many roots and shoots - composed of longitudinal cell files that differentiate into distinct tissues while maintaining their relative positions. Assuming quasi-static growth proportional to local elastic strain, and allowing each shell to possess distinct elastic and growth properties, we develop a novel, analytically tractable framework for exploring the coupling between growth and elasticity. To demonstrate the framework, we analyze a minimal two-layer model representing the epidermis and inner tissues. We use this model to explore the "epidermal growth control" hypothesis (1, 22), which states that the epidermis acts as a mechanical constraint on growth by regulating expansion and limiting inner tissue elongation.

A single morphoelastic rod

We begin by describing the shape kinematics of an axially growing morphoelastic rod which is homogeneous in all elastic and growth related properties. Building on previous models (8, 12, 21), the rod geometry is depicted using its centerline $\boldsymbol{r}(s,t)$, parametrized by its arc-length s and time t, as well as a local orthonormal material frame $\{\hat{\mathbf{e}}_1(s,t),\hat{\mathbf{e}}_2(s,t),\hat{\mathbf{e}}_3(s,t)\}$ (13, 23). Material points around the centerline are described using a vector on the local cross section $\boldsymbol{x} = x_1\hat{\mathbf{e}}_1 + x_2\hat{\mathbf{e}}_2$, and the shape of the cross section is assumed to be planar and constant (see Fig. 1B). Assuming the rod is twistless and shearless allows us to identify the tangent to the centerline $\partial\boldsymbol{r}/\partial s = \hat{\mathbf{t}}$ as a material frame vector $\hat{\mathbf{t}} = \hat{\mathbf{e}}_3$ and define the curvature or Darboux vector as $\boldsymbol{\kappa}(s,t) = \hat{\mathbf{t}} \times \partial\hat{\mathbf{t}}/\partial s = \kappa_1\hat{\mathbf{e}}_1 + \kappa_2\hat{\mathbf{e}}_2$. The shape kinematics is then fully described by the axial-axial component of the deformation rate tensor $\mathbf{d}$, which we term the axial strain rate and denote using $\dot{\varepsilon} \equiv \hat{\mathbf{t}} \cdot \mathbf{d}\hat{\mathbf{t}}$ (see details in supplementary information). Denoting co-rotating material time derivatives using $\dot{x} \equiv dx/dt$ such that $\dot{\boldsymbol{\kappa}} = \dot{\kappa}_1\hat{\mathbf{e}}_1 + \dot{\kappa}_2\hat{\mathbf{e}}_2$, and assuming small curvatures such that $|\boldsymbol{\kappa} \times \boldsymbol{x}| \ll 1$ for all points on the cross section, we found that the axial stain rate is linear within the cross section:

$$\dot{\varepsilon}(s,\boldsymbol{x},t) \approx \dot{\varepsilon}^0(s,t) + \dot{\kappa}_1(s,t)x_2 - \dot{\kappa}_2(s,t)x_1 \qquad \textbf{(1)}$$

where $\dot{\varepsilon}^0$ is the midline growth rate, and the linear terms are related the curvature rate $\dot{\boldsymbol{\kappa}}$ (see SI for demonstration). We now assume that the apparent shape of the rod may differ from its intrinsic shape, resulting in elastic deformations.

DRAFT

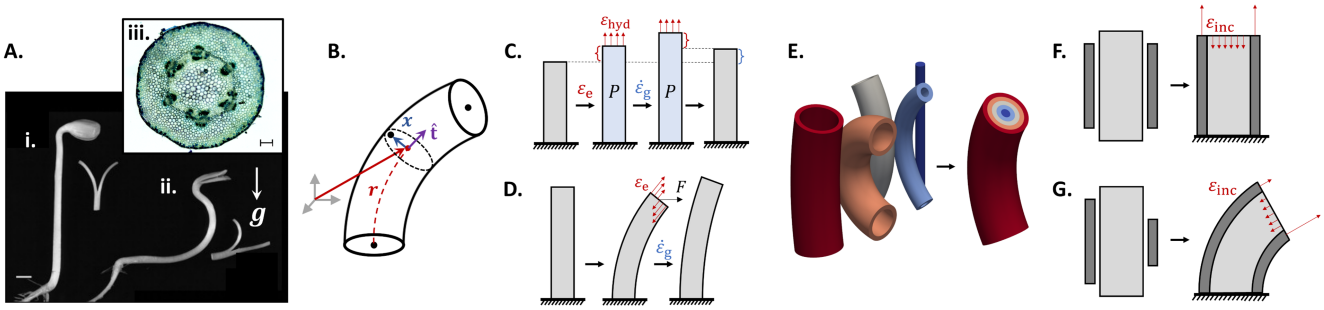

Fig. 1. A. Biological motivation. i.-ii. Photograph of 4-day-old etiolated sunflower seedlings and hypocotyl segments that were split longitudinally and placed for 1h into water. i. maintained vertically or ii. placed for 3h in horizontal position to induce gravitropic upward bending. The split halves curved outward, reflecting non-trivial residual stresses. $\boldsymbol{g}$ is the direction of gravity, scale bar=5mm. Taken from (1). iii. A cross section of a sunflower hypocotyl, showing concentric arrangement of various tissues. Image courtesy of Ahron Kempinski, scale bar 0.2mm. **B. Geometry.** A morphoelastic rod is defined by its moving centerline $\boldsymbol{r}(s,t)$ defined in arc length s and time t, as well as a local material frame $\{\hat{\mathbf{e}}_1(s,t),\hat{\mathbf{e}}_2(s,t),\hat{\mathbf{e}}_3(s,t)\}$ (not shown). We define the cross section of the rod A as the set of material points perpendicular to the tangent to the centerline $\hat{\mathbf{t}}(s,t)=\partial\boldsymbol{r}(s,t)/\partial s=\hat{\mathbf{e}}_3(s,t)$, effectively assuming a shearless rod, and span the cross section using the vector $\boldsymbol{x}(s,t)=x_1\hat{\mathbf{e}}_1(s,t)+x_2\hat{\mathbf{e}}_2(s,t)$. **C. Morphoelasticity.** Elastic strain (ε_{e}) in response to internal hydrostatic turgor pressure (P) elongates the tissue, while growth ($\dot{\varepsilon}_{\mathrm{g}}$) increases the intrinsic length of the organ - both contributing to the total observed deformation. **D. Intrinsic curvature dynamics.** Axial strain-based growth ($\dot{\varepsilon}_{\mathrm{g}}$) in the presence of elastic bending deformations (ε_{e}) induces changes in the intrinsic curvature. Here, bending results from an external force F. **E. Bundle of concentric shells.** To model the kinematics of an organ with internal residual stress, we use N connected uniform concentric cylindrical shells which grow together and constrain each other elastically. **F-G. Elastic strain due to structural incompatibility,** $\varepsilon_{\mathrm{inc}}$. Each illustration depicts a section of a bundle composed of two concentric shells, as in (E). **F.** Typical residual stress profile in rod-like plant organs, where the epidermis is under tension and the inner tissue is relatively compressed. This profile may also arise from differential stiffness (see Eq. 53 in the SI). **G.** Differential axial growth, superimposed on the residual strain profile in (F), produces bending and results in an asymmetric distribution of residual strain.

For simplicity, we restrict the discussion to bending and stretching deformations, assuming no elastic shear or twist, thus considering only axial stresses, denoted by the Cauchy stress tensor $\boldsymbol{\sigma}=\sigma\hat{\mathbf{t}}\otimes\hat{\mathbf{t}}$ (24). Taking a coarse-grained approach (3, 25, 26), we assume linear elasticity and write:

$$\sigma(s,\boldsymbol{x},t)=E(s,\boldsymbol{x},t)\varepsilon_e(s,\boldsymbol{x},t) \tag{2}$$

where ε_e is the axial strain and E is an effective Young's modulus describing tissue-scale elastic behavior. For simplicity, we constrain E to be time-independent and axisymmetric such that $E(s,\boldsymbol{x},t)=E(s,|\boldsymbol{x}|)$, and assume its first moment on each cross section nullifies.

Strain-based growth leads to stress relaxation. Due to the internal hydrostatic pressure within living plants cells, the stiff walls surrounding each cells are typically under tension. Since viscoelastic relaxation occurs on much shorter timescales than growth, which proceeds via slow, creep-like deformation, we assume quasi-static shape dynamics (13). The total axial strain rate can then be decomposed to a sum of the relative growth rate $\dot{\varepsilon}_{\mathrm{g}}$ and the quasi-static variations of axial elastic strain $\dot{\varepsilon}_{\mathrm{e}}$ via $\dot{\varepsilon}=\dot{\varepsilon}_{\mathrm{g}}+\dot{\varepsilon}_{\mathrm{e}}$ (13, 27) (see Fig. 1C). In plants, the axial relative growth rate of cells is commonly described by the Lockhart model, which captures the anisotropic elongation of cell walls driven by internal hydrostatic turgor pressure P (26, 28–30). Following recent generalizations of this model (13, 31–33), we adopt a strain-based growth formulation in which the axial growth rate is proportional to the axial elastic strain in the cell wall. Specifically, we use the relation:

$$\dot{\varepsilon}_{\mathrm{g}}=\phi(\varepsilon_{\mathrm{e}}-\varepsilon_{\mathrm{y}})_+ \tag{3}$$

where ϕ is the effective extensibility (with units 1/time), ε_{y} is the yield strain, and $(x)_+=x\Theta(x)$ where Θ is the Heaviside function. The total axial strain rate can then be written as:

$$\dot{\varepsilon}=\dot{\varepsilon}_{\mathrm{g}}+\dot{\varepsilon}_{\mathrm{e}}=\phi(\varepsilon_{\mathrm{e}}-\varepsilon_{\mathrm{y}})_++\dot{\varepsilon}_{\mathrm{e}} \tag{4}$$

If the strain rate $\dot{\varepsilon}$ is known, Eq. 4 represents a differential equation for ε_{e}. For example, a uniform morphoelastic organ growing axially under geometrical confinement acts elastically as a loaded column with constant length and $\dot{\varepsilon}=0$. Assuming no arc-length dependence, $\varepsilon_{\mathrm{e}}(t=0)=\varepsilon_{e,0}>\varepsilon_{\mathrm{y}}$, and no buckling, Eq. 4 gives $\varepsilon_e(t)=\varepsilon_{\mathrm{y}}+(\varepsilon_{e,0}-\varepsilon_{\mathrm{y}})e^{-\phi t}$, such that the elastic strain decays exponentially to its yield threshold (34). As for the dynamics of intrinsic curvature $\boldsymbol{\kappa}^0$, in the SI we show that Eqs. 1,2,4 give:

$$\dot{\boldsymbol{\kappa}}^0=\phi(\boldsymbol{\kappa}-\boldsymbol{\kappa}^0) \tag{5}$$

such that the intrinsic curvature $\boldsymbol{\kappa}^0$ relaxes to its actual curvature $\boldsymbol{\kappa}$ in the presence of external forces, as assumed in (35) (see Fig. 1D). In case the growth parameters ϕ or ε_{y} are not uniform across the rod section, additional terms may appear in the curvature dynamics (see SI). For example, setting $\varepsilon_{\mathrm{y}}=\varepsilon_{\mathrm{y}}^0+x_1\partial\varepsilon_{\mathrm{y}}/\partial x_1$ allows on side to grow faster in response to elastic strain, giving:

$$\dot{\boldsymbol{\kappa}}^0=\phi(\boldsymbol{\kappa}-\boldsymbol{\kappa}^0)+\phi\frac{\partial\varepsilon_{\mathrm{y}}}{\partial x_1}\hat{\mathbf{e}}_2 \tag{6}$$

Gradients in extensibility or yield strain can be used to model plant tropisms, where plants redirect their growth in the direction of external stimuli (12, 36). Equations 4–6 show that, in the absence of residual stresses, a strain-based growth model leads to stress relaxation toward steady-state values determined by external forces and differential growth parameters. As we show next, when residual stresses are present, these steady-state values also depend on the rod's internal inhomogeneity.

A bundle of N concentric morphoelastic cylindrical shells

Model assumptions. We now model the rod-like growing organ as a bundle of N connected, concentric cylindrical shells (see Fig. 1E), each representing a distinct tissue layer. While elastic and growth-related parameters may vary between shells, we assume that within each shell these properties are uniform, and that axial growth is compatible and follows Eq.4. Although the bundle grows freely - without external loads - the shells are mechanically coupled in parallel. This simulates symplastic growth, in which connected plant cells expand cohesively, without slippage between cells nor tissue layers. For each shell i we therefore decompose the elastic strain (or stress) into two additive contributions:

$$\varepsilon_{\mathrm{e},i} = \varepsilon_{\mathrm{hyd}} + \varepsilon_{\mathrm{inc},i} \tag{7}$$

where $\varepsilon_{\mathrm{hyd}}$ are reaction strains to the internal hydrostatic turgor pressure and $\varepsilon_{\mathrm{inc}}$ are residual strains caused by structural incompatibility (see Fig. 1F,G). Based on the assumptions of linear elasticity and a constant cross-section, we found that for constant turgor pressure P, $\varepsilon_{\mathrm{hyd}}$ is constant on the cross section and equals $P/\langle E\rangle$ where $\langle E\rangle$ is the average tissue-scale (bulk) stiffness of the cross section upon pressurization (see SI). For simplicity, we make the following additional assumptions : (i) the curvature of each shell is uniform along its length; (ii) the problem is two dimensional: the plane of curvature is on the (x_1, s) plane (namely, its intrinsic curvature vectors is parallel or anti-parallel to $\hat{\mathbf{e}}_2$), and the (x_1, s) plane coincides with a principle axis of its cross section; and (iii) the elastic deformations are small ($\varepsilon_{\mathrm{e}} \ll 1$). Under these assumptions, the elastic strain of each shell expressed in Eq. 7 can be decomposed to stretching and bending contributions:

$$\varepsilon_{\mathrm{e},i}(x_1,t) = \varepsilon^0_{\mathrm{e},i}(t) - x_1\left(K(t) - \kappa^0_i(t)\right) \tag{8}$$

where $\varepsilon^0_{\mathrm{e},i}$ is the average elastic axial strain of shell i, κ^0_i is its intrinsic curvature, and K is the actual curvature of the bundle, which acts as the actual curvature of each concentric shell. The elastic energy of the organ per unit arc length can be approximated by the integral $\frac{1}{2}\iint E\varepsilon^2_{\mathrm{e},i}da$ on the cross section of each concentric shell. Since E is axisymmetric this gives:

$$U = \frac{1}{2}\sum_{i=1}^{N}\left(E_iI_i(\kappa^0_i - K)^2 + E_iA_i(\varepsilon^0_{\mathrm{e},i})^2\right) \tag{9}$$

where E_i is the effective Young's modulus of shell i, I_i is its relevant second moment of area, and A_i is the area of its cross section.

Curvature dynamics. To express the shape dynamics, we begin with the rod's curvature. Since the shells are concentric, the axial strain of each rod $\varepsilon^0_{\mathrm{e},i}$ doesn't depend on the bundle's curvature K, and minimizing of the energy by K gives its intrinsic value K^0:

$$\frac{dU}{dK} = 0 \;\rightarrow\; K^0 = \frac{\sum_{i=1}^{N} E_iI_i\kappa^0_i}{\sum_{j=1}^{N} E_jI_j} \equiv \sum_{i=1}^{N} p^b_i\kappa^0_i \tag{10}$$

where in the last equality we define:

$$p^b_i \equiv \frac{E_iI_i}{\sum_{j=1}^{N} E_jI_j} \tag{11}$$

as the elastic bending weight of shell i, such that $0 \le p^b_i \le 1$ and $\sum_{i=1}^{N} p^b_i = 1$. In the absence of external forces the bundle assumes the curvature K^0 such that $K = K^0$, and residual stress may appear within the bundle as the intrinsic curvatures of individual shells $\{\kappa^0_i\}$ aren't necessarily compatible with K^0. Following Eq. 5, the dynamics of intrinsic curvature of each shell are given by:

$$\dot{\kappa}^0_i = \phi_i(K^0 - \kappa^0_i) = \phi_i\left(\sum_{j=1}^{N} p^b_j\kappa^0_j - \kappa^0_i\right) \tag{12}$$

where in the second equality we substituted Eq. 10. We solve these dynamics after introducing the dynamics of the average strain rate.

Axial growth dynamics. The dynamics of the average strain rate and the average elastic strain in each shell are given by Eq. 4:

$$\dot{\varepsilon}^0 = \phi(\varepsilon^0_{\mathrm{e},i} - \varepsilon_{\mathrm{y},i})_+ + \dot{\varepsilon}_{\mathrm{e},i} \tag{13}$$

where the average strain rate $\dot{\varepsilon}^0$ is assumed to be constant across each cross section, keeping the cross sections planar (as in Eq. 1). To continue, we now express $\dot{\varepsilon}^0$ using an averaged sum of the growth rates of the individual shells. For this, we first note that the sum of residual stresses within the organ vanishes, which from symmetry can be applied to each cross section via:

$$\sum_{i=1}^{N} E_iA_i\varepsilon^0_{\mathrm{inc},i} = 0 \tag{14}$$

where $\varepsilon^0_{\mathrm{inc},i}$ is the average incompatible strain in shell i. We then express the hydrostatic elastic strain, which is constant across the section, using:

$$\varepsilon_{\mathrm{hyd}} = \frac{\sum_{i=1}^{N} E_iA_i(\varepsilon^0_{\mathrm{e},i} - \varepsilon^0_{\mathrm{inc},i})}{\sum_{j=1}^{N} E_jA_j} \equiv \sum_{i=1}^{N} p^s_i\varepsilon^0_{\mathrm{e},i} \tag{15}$$

where in the first equation we substitute Eq. 7, and in the second equation we use Eq.14 and define:

$$p^s_i \equiv \frac{E_iA_i}{\sum_{j=1}^{N} E_jA_j} \tag{16}$$

as the elastic stretch weight of shell i, such that $0 \le p^s_i \le 1$ and $\sum_{i=1}^{N} p^s_i = 1$. Multiplying Eq. 13 by p^s_i and summing over the N shells gives the actual strain rate:

$$\dot{\varepsilon}^0 = \sum_{i=1}^{N} \phi_i p^s_i\left(\varepsilon_{\mathrm{hyd}} + \varepsilon^0_{\mathrm{inc},i} - \varepsilon_{y,i}\right) + \dot{\varepsilon}_{\mathrm{hyd}} \tag{17}$$

where the sum of the time derivatives of the residual axial elastic strains nullifies following Eq. 14. For brevity, we denote the elastic strain that drives growth by:

$$\delta\varepsilon_i \equiv \varepsilon^0_{\mathrm{e},i} - \varepsilon_{\mathrm{y},i} = \varepsilon_{\mathrm{hyd}} + \varepsilon^0_{\mathrm{inc},i} - \varepsilon_{\mathrm{y},i} \tag{18}$$

Using this notation, substituting Eq. 17 in Eq. 13 allows to write the dynamics of the axial elastic strain of shell i as:

$$\delta\dot{\varepsilon}_i = \sum_{j=1}^{N} \phi_j p_j^s \delta\varepsilon_j - \phi_i \delta\varepsilon_i + \dot{\varepsilon}_{\text{hyd}} - \dot{\varepsilon}_{\text{y},i} \tag{19}$$

Solving the dynamics. The dynamics of the curvature and average axial strain rate of the concentric shells depicted in Eqs. 12,19 can each be written as N coupled ODEs. Denoting the vectors $\mathbf{v}_\kappa = \left(\kappa_1^0, ..., \kappa_N^0\right)^T$ and $\mathbf{v}_{\delta\varepsilon} = (\delta\varepsilon_1, ..., \delta\varepsilon_N)^T$ allows us to write Eqs. 12,19 as:

$$\dot{\mathbf{v}}_\kappa = \mathbf{M}_\kappa \mathbf{v}_\kappa + \mathbf{F}_\kappa \tag{20}$$

$$\dot{\mathbf{v}}_{\delta\varepsilon} = \mathbf{M}_{\delta\varepsilon} \mathbf{v}_{\delta\varepsilon} + \mathbf{F}_{\delta\varepsilon} \tag{21}$$

where $\mathbf{M}_\kappa$ and $\mathbf{M}_{\delta\varepsilon}$ are $N \times N$ matrices defined by the corresponding elastic weights (Eqs. 11,16) and shell extensibilities:

$$\mathrm{M}_{\kappa,ij} = \phi_i (p_j^b - \delta_{ij}) \tag{22}$$

$$\mathrm{M}_{\delta\varepsilon,ij} = \phi_j (p_j^s - \delta_{ij}) \tag{23}$$

where $i, j \in \{1, ..., N\}$ and δ_{ij} is the Kronecker delta. The dynamics defined by these matrices describe the quasi-static growth response to incompatibility-induced elastic strains, such that the steady-state values of curvature and axial elastic strain lie in the kernel of these matrices. The vectors $\mathbf{F}_\kappa$ and $\mathbf{F}_{\delta\varepsilon}$, which render the equations inhomogeneous, represent processes other than incompatibility that can shift the steady state, such as time-dependent growth parameters, variations in turgor pressure, or spatial gradients in growth parameters within a single shell:

$$\mathrm{F}_{\kappa,i} = \phi_i \frac{\partial \varepsilon_{\text{y},i}}{\partial x_1}, \;\; \mathrm{F}_{\delta\varepsilon,i} = \dot{\varepsilon}_{\text{hyd}} - \dot{\varepsilon}_{\text{y,i}} \tag{24}$$

as shown in Eqs. 6,19. The general solution to Eqs. 20,21 with constant matrices $\mathbf{M}_\kappa$ and $\mathbf{M}_{\delta\varepsilon}$ can be written as (37) (removing the subscripts for clarity):

$$\mathbf{v}(t) = e^{\mathbf{M}t}\mathbf{c} + \int_0^t e^{\mathbf{M}(t-t')}\mathbf{F}(t')dt' \tag{25}$$

where $\mathbf{c}$ are constant coefficients set by the initial conditions. Using the solutions given by Eq. 25, the elastic strain profile within each shell can be written using Eq. 8. Complications arise when the stiffness profiles and extensibilities are allowed to vary in time (see SI).

Coupling the epidermis and inner tissues ($\mathrm{N} = 2$)

To explore the model's predictions, we focus on the simplest case of two shells, which may represent the epidermis and inner tissue in a rod-like organ. Without loss of generality, we identify shell 1 with the inner tissues (denoted by in) and shell 2 with the epidermis (denoted by ep). For simplicity, in all of the following examples we assume $\mathbf{M}_\kappa$ and $\mathbf{M}_{\delta\varepsilon}$ are time independent so that the dynamics solution is always given by Eq. 25 (the relevant matrix exponentials $e^{\mathbf{M}t}$ for N=2 appear in the SI).

Strict strain-based growth results in exponential relaxation to a steady state. We begin by assuming the dynamics are set only by the incompatibility-induced elastic strains, such that $\mathbf{F}_\kappa = 0$ and $\mathbf{F}_{\delta\varepsilon} = 0$. In the axial growth dynamics, we find that the axial strains decay exponentially to steady state values:

$$\begin{pmatrix} \delta\varepsilon_1(t) \\ \delta\varepsilon_2(t) \end{pmatrix} = c_1 \begin{pmatrix} 1/\phi_1 \\ 1/\phi_2 \end{pmatrix} + c_2 \begin{pmatrix} 1/p_1^s \\ -1/p_2^s \end{pmatrix} e^{-(p_2^s\phi_1 + p_1^s\phi_2)t} \tag{26}$$

where c_1 and c_2 are integration constants set by the initial conditions. The actual strain rate is then given by Eq. 17:

$$\dot{\varepsilon}^0(t) = c_1 + c_2(\phi_1 - \phi_2)e^{-(p_2^s\phi_1 + p_1^s\phi_2)t} \tag{27}$$

For example, if $\delta\varepsilon_1(0) = \delta\varepsilon_2(0) = \varepsilon_{\text{hyd}} - \varepsilon_{\text{y}}$ and $\varepsilon_{\text{inc},1}(0) = \varepsilon_{\text{inc},2}(0) = 0$ we obtain:

$$\begin{pmatrix} c_1 \\ c_2 \end{pmatrix} = \frac{\varepsilon_{\text{hyd}} - \varepsilon_{\text{y}}}{p_1^s\phi_2 + p_2^s\phi_1} \begin{pmatrix} \phi_1\phi_2 \\ p_1^s p_2^s(\phi_1 - \phi_2) \end{pmatrix} \tag{28}$$

As a sanity check, we validate the steady state of this model against a model of a continuous, straight, inhomogeneous rod and find good agreement (see SI).

In the curvature dynamics, the solution also presents an exponential decay to steady state values. The dynamics of the rod's curvature are found by Eq. 10:

$$\begin{aligned} K(t) &= p_1^b\kappa_1^0(t) + p_2^b\kappa_2^0(t) = \\ &= c_1 + c_2 p_2^b \left(1 - \frac{\phi_1}{\phi_2}\right) e^{-(p_2^b\phi_1 + p_1^b\phi_2)t} \end{aligned} \tag{29}$$

where c_1 and c_2 are once more integration constants set by the initial conditions. Given the initial values of the intrinsic curvatures of the shells $(\kappa_{1,0}^0, \kappa_{2,0}^0)$ yields:

$$\begin{pmatrix} c_1 \\ c_2 \end{pmatrix} = \frac{1}{p_2\phi_1 + p_1\phi_2} \begin{pmatrix} p_1\phi_2\kappa_{1,0}^0 + p_2\phi_1\kappa_{2,0}^0 \\ p_1\phi_2(\kappa_{2,0}^0 - \kappa_{1,0}^0) \end{pmatrix} \tag{30}$$

Equations 29,30 show that as long as the two shells begin as incompatible with different intrinsic curvatures ($\kappa_{2,0}^0 \neq \kappa_{1,0}^0$) we have $c_2 \neq 0$ and the centerline decays exponentially to the curvature c_1.

These results show that incompatibility-induced elastic strains cause the shells to relax their axial stress to steady-state values, which are set by the initial condition, extensibilities and elastic weights.

Analysis of a self-similar axial growth profile driven by differential yield threshold. We now use our framework to model the axial growth rate profile found in straight roots. To obtain a relatively taut epidermis, we assume for simplicity that $\phi_{\text{ep}} = \phi_{\text{in}} \equiv \phi$ and that the dynamics are driven by a time dependent yield threshold of the inner tissues, such that $\mathrm{F}_{\delta\varepsilon,\text{ep}} = 0$ and $\mathrm{F}_{\delta\varepsilon,\text{in}}(t) = \dot{\varepsilon}_{\text{y,in}}(t) \neq 0$. These assumptions give:

$$\dot{\varepsilon}^0(t) = \phi(\varepsilon_{\text{hyd}} - \varepsilon_{\text{y}}^0) - \int_0^t p_{\text{in}}^s \phi \dot{\varepsilon}_{\text{y,in}}(t')dt' \tag{31}$$

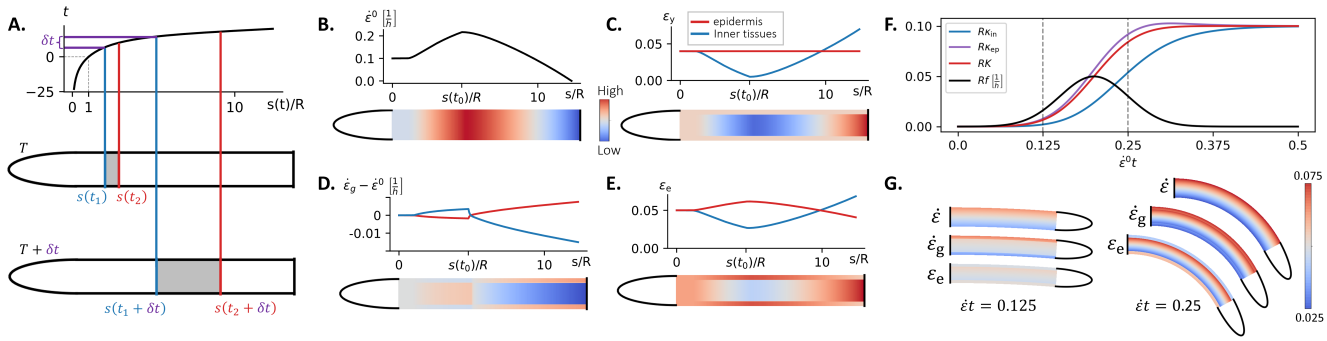

Fig. 2. Epidermis and inner tissue. A. Self-similar axial growth illustration. Top: As the whole organ expands symplastically, material points move along the organ length, changing their axial position (s) over time (t). In the case of self-similar growth, the time evolution of each point is described by bijection $s(t)$. Here we set $s(t=0)=R$. Since the fixed point at the apex is not moving ($v(s=0)=0$), $t\to-\infty$ as $s\to 0_+$. Bottom: the movement of two material points along the axis of the organ as described by $s(t)$. At time T, the points are located at $s_1=s(t_1)$ and $s_2=s(t_2)$. After a time interval δt, their new locations is given by $s_1=s(t_1+\delta t)$ and $s_2=s(t_2+\delta t)$. **B-E. Self-similar dynamics** of axial growth and elastic strain due to a differential yield threshold profile. The model is solved in time and plotted against arc-length $s(t)$, normalized by the cross section radius R. Below each graph the data is presented as a heatmap on an illustration of the organ. The parameter values used for this example are: $\phi=10$ 1/hour, $\varepsilon_{\text{hyd}}=0.05$, $\varepsilon^0_{\text{y,in}}=\varepsilon^0_{\text{y,ep}}=0.04$, $p^s_{\text{in}}=1/3$, $p^s_{\text{ep}}=2/3$, $a=0.05$, $b=0.5$, $t_0=14$ hours. **B**. The profile of actual strain rate mimics time-lapse measurements of cellular growth observed on the root. This growth dynamics can be obtained in the model by assuming specific profiles of yield threshold that differ between tissue layers (C). **C**. The given yield threshold which drives the dynamics, constant in the epidermis and varying in the inner tissues. **D**. The excess growth rate - meaning how much each tissue grows beyond the apparent strain rate - is equal to minus the variation of its elastic strain. **E**. The axial elastic strain resulting from yield incompatibilities between tissues. **F-G. Epidermal control of curvature. F**. The active curvature rate of the epidermis $f(t)$ leads to time dependent intrinsic curvatures which are incompatible with the actual curvature. These are plotted against the non dimensional time $\dot\varepsilon^0 t$ where $\dot\varepsilon^0$ is the constant axial growth rate of the centerline. The vertical dashed lines mark the times shown in G. **G**. The actual strain rate, growth rate and axial elastic strain of a bending organ depicted in F. At $\dot\varepsilon^0 t=0.125$, the curvature rate of the epidermis is shown and drives the curvature dynamics. At $\dot\varepsilon^0 t=0.25$, the elastic strain shows that due to incompatibility the inner tissues are elastically bent and the epidermis is elastically straightened, affecting the overall dynamics. The parameter values used for this example are: $\phi_{\text{in}}=\phi_{\text{ep}}=1$ 1/hour, $\varepsilon_{\text{hyd}}=0.05$, $\varepsilon^0_{\text{y,in}}=\varepsilon^0_{\text{y,ep}}=0$, $\dot\varepsilon^0=0.05$ 1/hour, $p^b_{\text{in}}=1/5$, $p^b_{\text{ep}}=4/5$, $f(t)=0.05\exp(-200(\dot\varepsilon^0 t-0.2)^2)$.

and:

$$\dot\varepsilon_{\text{g,ep}}(t)-\dot\varepsilon^0(t)=\int_0^t p^s_{\text{in}}\phi e^{-\phi(t-t')}\dot\varepsilon_{\text{y,in}}(t')dt' \tag{32}$$

$$\dot\varepsilon_{\text{g,in}}(t)-\dot\varepsilon^0(t)=-\int_0^t p^s_{\text{ep}}\phi e^{-\phi(t-t')}\dot\varepsilon_{\text{y,in}}(t')dt' \tag{33}$$

such that the excess growth $\dot\varepsilon_{\text{g},i}(t)-\dot\varepsilon^0(t)$ (which equals $-\dot\varepsilon^0_{\text{e},i}(t)$ following Eq. 13) is a convolution between the varying yield threshold $\dot\varepsilon_{\text{y,in}}(t)$ and an effective memory kernel with timescale $1/\phi$.

To enable comparison with experimental measurements, we assume the axial growth is self-similar, meaning the growth rate profile depends solely on the arc-length from the apex, denoted as $\dot\varepsilon^0(s)$, as is commonly done in root studies (16, 34, 38). Mathematically, this gives a self-similar velocity $ds/dt\equiv v(s)=\int^s\dot\varepsilon^0(s')ds'$ (14), such that material points are displaced axially according to the characteristic curve $t-\int^s ds'/v(s')=\text{const}$. Since the movement is unidirectional, a material point on the epidermis which is located at $s_0>0$ moves away from the apex and arrives after a time interval δt always to the same arc-length $s_0+\delta s$ (see Fig.2A). Without loss of generality, we now choose a specific $s_0>0$ and focus on the characteristic with $t(s_0)=0$, which gives a bijection $s=s(t)$. To express this bijection using the solution for the relative growth rate $\dot\varepsilon^0(t)$ found by our model (Eq. 31), we note that the strain rate can be related to the material point velocity via (14):

$$\dot\varepsilon^0(t)=\frac{dv}{ds}=\frac{dt}{ds}\frac{dv}{dt}=\frac{1}{v}\frac{dv}{dt} \tag{34}$$

where in the second equality we used the chain rule. Equation 34 allows to express the velocity as a function of time:

$$v(t)=v_0e^{\int_0^t\dot\varepsilon^0(t')dt'} \tag{35}$$

where v_0 is the velocity at $t=0$. Equation 35 allows to express the bijection via $s(s_0,t)-s_0=\int_0^t v(t')dt'$. As an example, to reproduce the triangular growth profile found in roots (34), we assume the yield threshold rate is a skewed triangular in time:

$$\text{f}_{\delta\varepsilon,\text{in}}(t)=\dot\varepsilon_{\text{y,in}}(t)=\begin{cases}-at/t_0 & t<t_0\\ b(t/t_0-1) & t\geq t_0\end{cases} \tag{36}$$

with $0<a<b$. This allows to solve the dynamics analytically. To simply the calculations, we assume $s(t=0)=R$ and that the growth rate between $0\leq s\leq R$ is constant and equals $\phi(\varepsilon_{\text{hyd}}-\varepsilon^0_{\text{y}})$. The results are plotted in Fig. 2B-E against arc-length. Initially, the lowering of the yield threshold of the inner tissue (Fig. 2C) both drives growth acceleration (Fig. 2B) and causes the inner tissues to accumulate relative compression, which is maintained for most of the dynamics (Fig. 2E). As the yield threshold of the inner tissues begins to increase, the signs of the integrals in Eqs. 32,33 are reversed and the epidermis grows faster than the inner tissues (Fig. 2D). This incrementally decreases the stretch of the epidermis, such that when growth ceases at the base, the epidermis is relatively compressed over a short arc length (Fig. 2E). Such relative compression may lead to a twist instability, as commonly appearing in mutant phenotypes between the growth zone and mature zone of roots (21, 39). This example

demonstrates how our framework allows to relate between possible morphoelastic action of morphgen patterns along the organ (here implemented effectively by $\varepsilon_{\mathrm{y,in}}(s)$), the apparent shape kinematics, and the residual stress pattern.

Epidermal control of curvature leads to mechanical "memory" and effective autotropism. We now model an epidermal control of curvature, assuming a constant axial strain rate. Specifically, we assume the epidermis reacts to a morphogen which does not affect the inner tissues, such that $\mathrm{F}_{\kappa,\mathrm{ep}}(t) = f(t) \neq 0$ and $\mathrm{F}_{\kappa,\mathrm{in}} = 0$. In this case, the inner tissues are bent due to the intrinsic curvature of the epidermis, and relax to their current curvature with rate ϕ_{in} (as in Eq. 5). The inner tissues therefore "lag" behind the epidermis in their intrinsic curvature, resulting in dynamic curvature incompatibility. Assuming the initial organ is straight with $K(0) = 0$, the resulting dynamics of the curvature of the rod can be written as:

$$K(t) = \frac{p_2^b \phi_1}{p_2^b \phi_1 + p_1^b \phi_2} \int_0^t f(t')dt' + \frac{p_1^b p_2^b (\phi_2 - \phi_1)}{p_2^b \phi_1 + p_1^b \phi_2} \int_0^t e^{-(p_2^b \phi_1 + p_1^b \phi_2)(t-t')} f(t')dt' \quad \textbf{(37)}$$

An example of this model is shown in Fig. 2F-G. To analyze the resulting dynamics, we take a time derivative of Eq. 37 which gives:

$$\dot{K} = p_{\mathrm{ep}}^b f(t) + p_{\mathrm{ep}}^b \phi_{\mathrm{in}} \int_0^t f(t')dt' - (p_{\mathrm{ep}}^b \phi_{\mathrm{in}} + p_{\mathrm{in}}^b \phi_{\mathrm{ep}}) K \quad \textbf{(38)}$$

The three additive terms in the right hand side of Eq. 38 can be interpreted as: (i) an immediate effect of the curvature rate of the epidermis, (ii) mechanical "memory" coming from the relaxation rate of the inner tissue (17), and (iii) effective autotropism (15, 16, 40). Autotropism is a growth induced straightening motion which acts alongside gravitropic responses in tilted shoots and roots. Though autotropism is often linked to active proprioception of the organ's own curvature, its underlying mechanisms remain unclear. The model in Eq. 38 raises the possibility that autotropism may result, at least in part, from residual stresses within the organ, with sensitivity:

$$\gamma = \frac{p_{\mathrm{ep}}^b \phi_{\mathrm{in}} + p_{\mathrm{in}}^b \phi_{\mathrm{ep}}}{\dot{\varepsilon}^0} = \\ = \frac{\phi_{\mathrm{ep}} \phi_{\mathrm{in}}}{\varepsilon_{\mathrm{hyd}} - \varepsilon_y} \left(\frac{p_{\mathrm{ep}}^b}{\phi_{\mathrm{ep}}} + \frac{p_{\mathrm{in}}^b}{\phi_{\mathrm{in}}} \right) \left(\frac{p_{\mathrm{ep}}^s}{\phi_{\mathrm{ep}}} + \frac{p_{\mathrm{in}}^s}{\phi_{\mathrm{in}}} \right) \quad \textbf{(39)}$$

where in the second equality we use the steady state strain rate given by Eqs. 27,28. For example, if $\phi_{\mathrm{in}} = \phi_{\mathrm{ep}}$ we obtain $\gamma_1 = 1/(\varepsilon_{\mathrm{hyd}} - \varepsilon_y)$. Alternatively, assuming a very stiff epidermis via $p_{\mathrm{ep}}^b = p_{\mathrm{ep}}^s = 1$ gives $\gamma_2 = \phi_{\mathrm{in}} \gamma_1 / \phi_{\mathrm{ep}}$. Then, assuming $\varepsilon_{\mathrm{hyd}} - \varepsilon_y \sim 0.1$ gives an order of magnitude of $\gamma_1 \sim 10$, which can be compared to the experimentally estimated $\gamma \sim 1$ found in roots (16).

To continue the analysis, we note that the steady state curvature of Eq. 38 at $t \to \infty$, assuming $f(t \to \infty) = 0$, can be written as:

$$K(t \to \infty) = \frac{p_{\mathrm{ep}}^b \phi_{\mathrm{in}}}{p_{\mathrm{ep}}^b \phi_{\mathrm{in}} + p_{\mathrm{in}}^b \phi_{\mathrm{ep}}} \int_0^\infty f(t')dt' \quad \textbf{(40)}$$

Equation 40 shows that after the active bending of the epidermis expressed by $f(t)$ ends, and as long as the growth-induced remodeling continues, the steady state curvature is set by the integral of the active curvature rate of the epidermis. A notable edge case of this model is the limit $\phi_{\mathrm{in}} \ll p_{\mathrm{in}}^b \phi_{\mathrm{ep}} / p_{\mathrm{ep}}^b$, which can be interpreted as the inner tissues remaining intrinsically straight throughout the dynamics. In this regime of the parameter space, the steady case curvature in Eq. 40 is approximately 0, such that the straight inner tissues act as a bending spring that pushes the epidermis to a straight steady state. We note that the intrinsically straight part of the organ mustn't be the inner tissues - for example, a similar mechanism was modeled in (41) by setting the steady state angles between cell walls as straight angles. In addition, this edge case may represent the role of cellular microfibrils in posture control as found experimentally in (42).

Conclusion

We introduce a novel mathematical framework that rigorously couples growth and elasticity in rod-like plant organs, enabling systematic investigation of how residual stresses contribute to macroscopic kinematics. Our model reveals that incompatibility-induced residual stresses — arising from mismatched intrinsic growth between tissues and common in turgid symplastic plant structures — can play a significant role in driving quasi-static plant movements. Furthermore, using connected morphoelastic cylindrical shells allows to express the dynamics analytically, strengthening intuition and facilitating hypotheses generation. We illustrate the versatility of this approach through two key models: one describing self-similar axial growth, and another capturing epidermis-driven curvature control. These models suggest that residual axial stresses may underlie phenomena such as root twisting, autotropism, and memory effects in plant responses (17). As the models offer quantitative predictions of dynamic parameters and spatio-temporal fields, they provide a foundation for future investigations into mechanochemical coupling in plant growth and its experimental validation. Within this framework, we emphasize that macroscopic residual stress patterns can be experimentally probed using peeling and splitting techniques (1, 43, 44). For example, applying our model of epidermal curvature control to a baseline state with a relatively taut epidermis (using Eq.8) yields a distinct, asymmetric stress distribution across the bent cross-section, as illustrated in Fig.1G. Notably, a similar stress pattern has been observed in experiments involving the peeling of plant shoots following a gravitropic response (44). Furthermore, we note that the residual stress profiles we describe here are not the only profiles that exist in rod-like organs and may affect the apparent curvature dynamics. For example, in (7, 8) radial incompatibility and gradients in turgor

pressure are shown to create non-trivial residual axial stress patterns in a rod-like organs. In addition, applying a different growth model which couples axial growth directly to hoop stresses leads to different kinematics, as shown in (45–48).

Future theoretical extensions to this model include: (i) breaking axial symmetry in the stiffness profile to simulate differential cell wall softening by morphogens; (ii) adding external stresses caused by weight and geometric confinement; (iii) allowing tissues to actively shorten or elongate differentially in response to elastic stress, as assumed in models of reaction wood; and (iv) allowing for changes in organ radius.

From a methodological perspective, our framework addresses an "inverse morphoelastic problem": Given an observed shape kinematics, a growth law which couples growth and elasticity, and the symmetries of the growing shape, what are the possible residual stress patterns that can drive the shape dynamics? Furthermore, can these be induced by the moprhogens patterns known to control development? Though we focus on rod-like organs, such theoretical investigations may help elucidate the possible role of residual stress in the shape dynamics and morphogenesis of organs with different symmetries, such as planar leaves, spherical onions or dome shaped apical meristems.

ACKNOWLEDGEMENTS

A.P. acknowledges support from the Gatsby Charitable Foundation (grant GAT3395/PR4B) and the Herchel Smith Fund, and thanks Yasmine Meroz, Anne-Lise Routier-Kierzkowska, Henrik Jönsson, Bruno Moulia, and Mathieu Rivière for their valuable comments, insightful discussions, and support.

Bibliography

1. U Kutschera and KJ Niklas. The epidermal-growth-control theory of stem elongation: an old and a new perspective. *Journal of plant physiology*, 164(11):1395–1409, 2007.
2. R Vandiver and A Goriely. Tissue tension and axial growth of cylindrical structures in plants and elastic tissues. *Europhysics Letters*, 84(5):58004, 2008.
3. Tobias I Baskin and Oliver E Jensen. On the role of stress anisotropy in the growth of stems. *Journal of experimental botany*, 64(15):4697–4707, 2013.
4. Enrico Coen and Daniel J Cosgrove. The mechanics of plant morphogenesis. *Science*, 379 (6631):eade8055, 2023.
5. Sylvia R Silveira, Loann Collet, Sahil M Haque, Luc Lapierre, Agnieszka Bagniewska-Zadworna, Richard S Smith, Frederick P Gosselin, Anne-Lise Routier-Kierzkowska, and Daniel Kierzkowski. Mechanical interactions between tissue layers underlie plant morphogenesis. *Nature Plants*, pages 1–15, 2025.
6. Benjamin P Lapointe, Neha Sharma Kaur, Anne-Lise Routier-Kierzkowska, and Agata Burian. From stress to growth: Mechanical tissue interactions in developing organs. *Current Opinion in Plant Biology*, 86:102759, 2025.
7. Hadrien Oliveri and Ibrahim Cheddadi. Hydromechanical field theory of plant morphogenesis. *Journal of the Mechanics and Physics of Solids*, 196:106035, 2025.
8. Derek E Moulton, Thomas Lessinnes, and Alain Goriely. Morphoelastic rods iii: Differential growth and curvature generation in elastic filaments. *Journal of the Mechanics and Physics of Solids*, 142:104022, 2020.
9. B Moulia and M Fournier. The power and control of gravitropic movements in plants: a biomechanical and systems biology view. *Journal of Experimental Botany*, 60(2):461–486, January 2009.
10. Sharon J Gerbode, Joshua R Puzey, Andrew G McCormick, and L Mahadevan. How the cucumber tendril coils and overwinds. *Science*, 337(6098):1087–1091, 2012.
11. Kristoffer Jonsson, Yuan Ma, Anne-Lise Routier-Kierzkowska, and Rishikesh P Bhalerao. Multiple mechanisms behind plant bending. *Nature Plants*, 9(1):13–21, 2023.
12. John A Fozard, Malcolm J Bennett, John R King, and Oliver E Jensen. Hybrid vertex-midline modelling of elongated plant organs. *Interface focus*, 6(5):20160043, 2016.
13. Alain Goriely. *The Mathematics and Mechanics of Biological Growth*. Springer, 2017.
14. Amir Porat, Fabio Tedone, Michele Palladino, Pierangelo Marcati, and Yasmine Meroz. A general 3d model for growth dynamics of sensory-growth systems: From plants to robotics. *Frontiers in Robotics and AI*, 7:89, 2020. ISSN 2296-9144. doi: 10.3389/frobt.2020.00089.
15. Renaud Bastien, Tomas Bohr, Bruno Moulia, and Stéphane Douady. Unifying model of shoot gravitropism reveals proprioception as a central feature of posture control in plants. *Proceedings of the National Academy of Sciences of the United States of America*, 110: 755–760, January 2013.
16. Amir Porat, Mathieu Rivière, and Yasmine Meroz. A quantitative model for spatio-temporal dynamics of root gravitropism. *Journal of Experimental Botany*, page erad383, 10 2023. ISSN 0022-0957. doi: 10.1093/jxb/erad383.
17. Mathieu Rivière and Yasmine Meroz. Revealing how memory shapes time-dependent computational processes in plant tropisms. *bioRxiv*, pages 2023–01, 2023.
18. Hadrien Oliveri, Derek E Moulton, Heather A Harrington, and Alain Goriely. Active shape control by plants in dynamic environments. *Physical Review E*, 110(1):014405, 2024.
19. Raghunath Chelakkot and L Mahadevan. On the growth and form of shoots. *Journal of The Royal Society Interface*, 14(128):20170001, March 2017.
20. Daniele Agostinelli, Alessandro Lucantonio, Giovanni Noselli, and Antonio DeSimone. Nutations in growing plant shoots: The role of elastic deformations due to gravity loading. *Journal of the Mechanics and Physics of Solids*, 136:103702, 2020. ISSN 0022-5096. doi: https://doi.org/10.1016/j.jmps.2019.103702. The Davide Bigoni 60th Anniversary Issue.
21. Amir Porat, Arman Tekinalp, Yashraj Bhosale, Mattia Gazzola, and Yasmine Meroz. On the mechanical origins of waving, coiling and skewing in arabidopsis thaliana roots. *Proceedings of the National Academy of Sciences*, 121(11):e2312761121, 2024.
22. Rosemary J Dyson, Gema Vizcay-Barrena, Leah R Band, Anwesha N Fernandes, Andrew P French, John A Fozard, T Charlie Hodgman, Kim Kenobi, Tony P Pridmore, Michael Stout, et al. Mechanical modelling quantifies the functional importance of outer tissue layers during root elongation and bending. *New Phytologist*, 202(4):1212–1222, 2014.
23. Stuart S Antman. Problems in nonlinear elasticity. *Nonlinear Problems of Elasticity*, pages 513–584, 2005.
24. L. M. Landau and E. M. Lifshitz. *Theory of Elasticity*. Pergamon Press, 1959.
25. Lorna J Gibson. Cellular solids. *Mrs Bulletin*, 28(4):270–274, 2003.
26. Oliver E Jensen. Theoretical tools and concepts for modelling growing plant tissues. *Soft Matter in Plants: From Biophysics to Biomimetics*, 15:85, 2022.
27. Efi Efrati, Eran Sharon, and Raz Kupferman. The metric description of elasticity in residually stressed soft materials. *Soft Matter*, 9(34):8187–8197, 2013.
28. James A. Lockhart. An analysis of irreversible plant cell elongation. *Journal of Theoretical Biology*, 8(2):264 – 275, 1965. ISSN 0022-5193. doi: https://doi.org/10.1016/0022-5193(65)90077-9.
29. Olivier Ali, Vincent Mirabet, Christophe Godin, and Jan Traas. Physical models of plant development. *Annual Review of Cell and Developmental Biology*, 30(1):59–78, 2014.
30. Jacques Dumais. Mechanics and hydraulics of pollen tube growth. *New Phytologist*, 232 (4):1549–1565, 2021.
31. Behruz Bozorg, Pawel Krupinski, and Henrik Jönsson. Stress and strain provide positional and directional cues in development. *PLoS computational biology*, 10(1):e1003410, 2014.
32. Gabriella Mosca, Ryan C Eng, Milad Adibi, Saiko Yoshida, Brendan Lane, Leona Bergheim, Gaby Weber, Richard S Smith, and Angela Hay. Growth and tension in explosive fruit. *Current Biology*, 34(5):1010–1022, 2024.
33. Valentin Laplaud, Elise Muller, Natalia Demidova, Stéphanie Drevensek, and Arezki Boudaoud. Assessing the hydromechanical control of plant growth. *Journal of the Royal Society Interface*, 21(214):20240008, 2024.
34. Manon Quiros, Marie-Béatrice Bogeat-Triboulot, Etienne Couturier, and Evelyne Kolb. Plant root growth against a mechanical obstacle: the early growth response of a maize root facing an axial resistance is consistent with the lockhart model. *Journal of the Royal Society Interface*, 19(193):20220266, 2022.
35. Raymond E. Goldstein and Alain Goriely. Dynamic buckling of morphoelastic filaments. *Phys. Rev. E*, 74:010901, Jul 2006. doi: 10.1103/PhysRevE.74.010901.
36. Rosemary J. Dyson, Gema Vizcay-Barrena, Leah R. Band, Anwesha N. Fernandes, Andrew P. French, John A. Fozard, T. Charlie Hodgman, Kim Kenobi, Tony P. Pridmore, Michael Stout, Darren M. Wells, Michael H. Wilson, Malcolm J. Bennett, and Oliver E. Jensen. Mechanical modelling quantifies the functional importance of outer tissue layers during root elongation and bending. *New Phytologist*, 202(4):1212–1222, 2014. doi: https://doi.org/10.1111/nph.12764.
37. William E Boyce, Richard C DiPrima, and Douglas B Meade. *Elementary differential equations and boundary value problems*. John Wiley & Sons, 2021.
38. Tobias I Baskin, Simon Preston, Ellen Zelinsky, Xiaoli Yang, Melissa Elmali, Dimitrios Bellos, Darren M Wells, and Malcolm J Bennett. Positioning the root elongation zone is saltatory and receives input from the shoot. *Iscience*, 23(7), 2020.
39. Renate Weizbauer, Winfried S Peters, and Burkhard Schulz. Geometric constraints and the anatomical interpretation of twisted plant organ phenotypes. *Frontiers in plant science*, 2: 62, 2011.
40. Renaud Bastien, Stĕphane Douady, and Bruno Moulia. A unifying modeling of plant shoot gravitropism with an explicit account of the effects of growth. *Frontiers in Plant Science*, 5, April 2014.
41. Petra Žádníková, Krzysztof Wabnik, Anas Abuzeineh, Marçal Gallemi, Dominique Van Der Straeten, Richard S Smith, Dirk Inzé, Jiří Friml, Przemysław Prusinkiewicz, and Eva Benková. A model of differential growth-guided apical hook formation in plants. *The Plant Cell*, 28(10):2464–2477, 2016.
42. Keishi Okamoto, Haruko Ueda, Tomoo Shimada, Kentaro Tamura, Takehide Kato, Masao Tasaka, Miyo Terao Morita, and Ikuko Hara-Nishimura. Regulation of organ straightening and plant posture by an actin–myosin xi cytoskeleton. *Nature plants*, 1(4):1–7, 2015.
43. J Van Overbeek and FW Went. Mechanism and quantitative application of the pea test. *Botanical Gazette*, 99(1):22–41, 1937.
44. Zygmunt Hejnowicz and Andreas Sievers. Tissue stresses and their graviresponsive changes in stems of reynoutria japonica houtt. *Journal of plant physiology*, 149(1-2):91–101, 1996.
45. Jacques Dumais, Sidney L Shaw, Charles R Steele, Sharon R Long, and Peter M Ray. An anisotropic-viscoplastic model of plant cell morphogenesis by tip growth. *The International journal of developmental biology*, 2006.
46. Felix Wong, Lars D Renner, Gizem Özbaykal, Jayson Paulose, Douglas B Weibel, Sven Van Teeffelen, and Ariel Amir. Mechanical strain sensing implicated in cell shape recovery in escherichia coli. *Nature microbiology*, 2(9):1–8, 2017.
47. Salem Al Mosleh, Ajay Gopinathan, and Christian Santangelo. Growth of form in thin elastic structures. *Soft matter*, 14(41):8361–8371, 2018.
48. Ankit Walia, Rainer Waadt, and Alexander M Jones. Genetically encoded biosensors in plants: pathways to discovery. *Annual Review of Plant Biology*, 69:497–524, 2018.
49. Jerrold E Marsden and Thomas JR Hughes. *Mathematical foundations of elasticity*. Courier

Corporation, 2012.
50. M Gazzola, LH Dudte, A McCormick, and L Mahadevan. Forward and inverse problems in the mechanics of soft filaments. *Royal Society Open Science*, 5(6), 2018.
51. Thomas Lessinnes, Derek E Moulton, and Alain Goriely. Morphoelastic rods part ii: growing birods. *Journal of the Mechanics and Physics of Solids*, 100:147–196, 2017.

Morphoelastic rods: state-of-the-art

Shape dynamics. The position vector of each point in the rod $\boldsymbol{p}$ can be written as (see Fig. 1B):

$$\boldsymbol{p}(x_1,x_2,s,t) = \boldsymbol{r}(s,t) + x_1\hat{\mathbf{e}}_1(s,t) + x_2\hat{\mathbf{e}}_2(s,t) \quad \textbf{(41)}$$

where the cross sections are bound to move together as solid planes. To let the rod grow axially, we use the arc-length of the rod at time $t=0$ denote by S_0 as a material coordinate, let the actual arc length develop in time via $s=s(S_0,t)$ and define the axial stretch as $\lambda(s,t)=\partial s/\partial S_0$. Using 41, the metric in the rod with respect to the coordinate system (x_1,x_2,S_0) is then (omitting the dependencies for brevity):

$$\boldsymbol{g} = \mathrm{diag}\left(1,1,\lambda^2(1+\kappa_1x_2-\kappa_2x_1)^2\right) \quad \textbf{(42)}$$

Since the deformations are shearless, the material frame remains congruent to the principal strain directions. Therefore, the deformation rate tensor can be found by taking the material time derivative of the metric from Eq. 42 (49). Denoting $\dot{X}\equiv dX/dt$, this gives in the orthonormal basis (12):

$$\mathbf{d} = \frac{1}{2}\dot{\boldsymbol{g}}\boldsymbol{g}^{-1} = \left(\frac{\dot{\lambda}}{\lambda}+\frac{\dot{\kappa}_1x_2-\dot{\kappa}_2x_1}{1+\kappa_1x_2-\kappa_2x_1}\right)\hat{\mathbf{t}}\otimes\hat{\mathbf{t}} \quad \textbf{(43)}$$

Using the logarithmic strain measure $\varepsilon^0=\ln(\lambda)$ and assuming small curvature $R|\boldsymbol{\kappa}|\ll 1$ gives Eq. 1 from the main text.

Rod mechanics. Separation of timescales between slow growth and fast elastic relaxations allows us to assume quasi static growth (13). Mechanical equilibrium is then expressed by the time independent Cosserat rod equations along the centerline (23, 50):

$$\frac{\partial\boldsymbol{n}}{\partial s}+\boldsymbol{f}=0 \quad \textbf{(44)}$$

$$\frac{\partial\boldsymbol{m}}{\partial s}+\frac{\partial\boldsymbol{r}}{\partial s}\times\boldsymbol{n}+\boldsymbol{c}=0 \quad \textbf{(45)}$$

where $\boldsymbol{n}$ are the internal contact forces, $\boldsymbol{m}$ are the internal torques or bending moments, $\boldsymbol{f}$ are the external forces per unit length and $\boldsymbol{c}$ are the external couples per unit length, all functions of s and t. Since in our model the cross sections remain planar, the internal contact forces and bending moments can be expressed using the 0-th and 1st moments of the axial stress (23, 51):

$$\boldsymbol{n} = \mathbf{S}(\varepsilon_e^0\hat{\mathbf{t}}) = \iint_A \boldsymbol{\sigma}d\boldsymbol{a} \quad \textbf{(46)}$$

$$\boldsymbol{m} = \mathbf{B}\left(\boldsymbol{\kappa}-\boldsymbol{\kappa}^0\right) = \iint_A \boldsymbol{x}\times(\boldsymbol{\sigma}d\boldsymbol{a}) \quad \textbf{(47)}$$

where $d\boldsymbol{a}=da\hat{\mathbf{t}}$ is an infinitesimal area vector on the cross section, and $\mathbf{S}$ and $\mathbf{B}$ are stiffness matrices which are diagonal in the local material coordinates, where $\mathrm{S}_{33}=\iint_A Eda\equiv\langle E\rangle A$, denoting $\langle E\rangle$ as the average axial stiffness of the cross section, and $\mathrm{B}_{11}=\iint_A Ex_2^2da$ and $\mathrm{B}_{22}=\iint_A Ex_1^2da$ are the second moments of the axial stiffness (second moment of area).

By definition, the sum of residual stresses within the organ vanishes, which from symmetry can be applied to each cross section:

$$\iint_A \sigma_{\mathrm{inc}}da = \iint_A E\varepsilon_{\mathrm{inc}}da = 0 \quad \textbf{(48)}$$

The reaction strain to the inner hydorstatic pressure can be derived from Eq. 46 assuming the turgor pressure P is constant:

$$\varepsilon_{\mathrm{hyd}} = \frac{\iint_A \sigma_{\mathrm{hyd}}da}{\mathrm{S}_{33}} = \frac{P}{\langle E\rangle} \quad \textbf{(49)}$$

Intrinsic curvature dynamics. Following (8), or by substituting Eqs. 1,2,4 in the time derivative of Eq. 47, the dynamics of intrinsic curvature can be written as:

$$\dot{\boldsymbol{\kappa}}^0 = \dot{\kappa}_1^0\hat{\mathbf{e}}_1+\dot{\kappa}_2^0\hat{\mathbf{e}}_2 = \mathbf{B}^{-1}\iint_A \boldsymbol{x}\times\left(E\dot{\varepsilon}_{\mathrm{g}}d\boldsymbol{a}\right) \quad \textbf{(50)}$$

Substituting the strain-based growth law from Eq. 3 in Eq. 50 result in Eqs. 5,6 in the main text.

Residual stress in a straight inhomogeneous rod

Here, we investigate the steady state of a free, straight rod growing axially with a constant strain rate $\dot{\varepsilon}=\dot{\varepsilon}^0>0$. To avoid changes in the intrinsic curvature of the rod, we assume the elastic and growth parameters of the rod are axis symmetric, such that the rod is inhomogeneous only with respect to the radial distance form the axis $x=|\boldsymbol{x}|$. In addition, we assume the elastic strain profile of the rod is constant yet not necessarily homogeneous with $\dot{\varepsilon}_{\mathrm{e}}=0$. The elastic strain can then be expressed by inverting Eq. 4:

$$\varepsilon_{\mathrm{e}}(x) = \varepsilon_{\mathrm{y}}(x)+\frac{\dot{\varepsilon}^0}{\phi(x)} = \varepsilon_{\mathrm{hyd}}+\varepsilon_{\mathrm{inc}}(x) \quad \textbf{(51)}$$

where the last equality comes from Eq. 7. Equation 51 shows that differential yield strain ε_{y} or extensibility ϕ vary the local steady-state elastic strain and corresponding intrinsic length. The possible profiles of these growth parameters are constrained by the condition for mechanical equilibrium, which can be found by integrating Eq. 51 multiplied by the local stiffness $E(x)$ across the cross section and substituting Eqs. 48-49:

$$\iint_A E(x)\left(\varepsilon_{\mathrm{y}}(x)+\frac{\dot{\varepsilon}^0}{\phi(x)}\right)da = P \quad \textbf{(52)}$$

This model agrees with the steady state predicted by Eqs. 26-28 in a piecewise manner: substituting the steady state growth rate c_1 from Eq. 28 in Eq. 26 reproduces Eq. 51, as well as Eq. 52 via $p_1^s(\delta\varepsilon_1+\varepsilon_{\mathrm{y}})+p_2^s(\delta\varepsilon_2+\varepsilon_{\mathrm{y}})=\varepsilon_{\mathrm{hyd}}$.

We note that this model allows to describe the local relative

residual stress, which we define by the difference between the axial stress to its average value P (Eq. 52):

$$\sigma_{\text{rel}}(x) = \sigma(x) - P = E(x)\left(\varepsilon_{\text{hyd}} + \varepsilon_{\text{inc}}(x)\right) - P = \\ = \left(\frac{E(x)}{\langle E \rangle} - 1\right) P + E(x)\varepsilon_{\text{inc}}(x) \quad \textbf{(53)}$$

where in the last equality we used Eq. 49. Equation 53 shows that the relative stress can result from two different additive mechanisms (3): (i) turgor pressure, which distributes stress unevenly as in parallel springs: if the local stiffness is higher (smaller) than the average stiffness, the tissue is relatively taut (compressed); and (ii) growth induced length incompatibility, which as shown Eq. 51 can be attributed to differential growth parameters.

Matrix exponentials used in the main text

In the case $N = 2$, the matrices given by Eqs. 22,23 give:

$$e^{\mathbf{M}_{\delta\varepsilon} t} = \\ = \frac{\begin{pmatrix} p_1^s\phi_2 + p_2^s\phi_1 e^{-(p_2^s\phi_1 + p_1^s\phi_2)t} & p_2^s\phi_2 - p_2^s\phi_2 e^{-(p_2^s\phi_1 + p_1^s\phi_2)t} \\ p_1^s\phi_1 - p_1^s\phi_1 e^{-(p_2^s\phi_1 + p_1^s\phi_2)t} & p_2^s\phi_1 + p_1^s\phi_2 e^{-(p_2^s\phi_1 + p_1^s\phi_2)t} \end{pmatrix}}{p_2^s\phi_1 + p_1^s\phi_2} \quad \textbf{(54)}$$

$$e^{\mathbf{M}_{\kappa} t} = \\ = \frac{\begin{pmatrix} p_1^b\phi_2 + p_2^b\phi_1 e^{-(p_2^b\phi_1 + p_1^b\phi_2)t} & p_2^b\phi_1 - p_2^b\phi_1 e^{-(p_2^b\phi_1 + p_1^b\phi_2)t} \\ p_1^b\phi_2 - p_1^b\phi_2 e^{-(p_2^b\phi_1 + p_1^b\phi_2)t} & p_2^b\phi_1 + p_1^b\phi_2 e^{-(p_2^b\phi_1 + p_1^b\phi_2)t} \end{pmatrix}}{p_2^b\phi_1 + p_1^b\phi_2} \quad \textbf{(55)}$$

Note on Time-Dependent Stiffness

Although we do not solve the dynamics for time-dependent stiffness profiles $\{E_i\}$, we briefly note the complications such profiles introduce. First, both the elastic weights $\{p_i^b, p_i^s\}$ and the hydrostatic strain $\varepsilon_{\text{hyd}} = P/\langle E \rangle$ become time-dependent. Second, when deriving the axial strain dynamics, taking the time derivative of Eq. 14 produces two sums. This modifies Eq. 17 by adding the following extra term on the right-hand side:

$$\sum_{j=1}^{N} p_j^s \frac{\dot{E}_j}{E_j}\left(\varepsilon_{\text{hyd}} - \delta\varepsilon_j - \varepsilon_{\text{y},j}\right). \quad \textbf{(56)}$$

As a result, the updated matrices $\mathbf{M}$ becomes time-dependent, and the system can be solved using the fundamental matrix method (37). The same applies if the extensibilities $\{\phi_i\}$ are time-dependent.